# Pattern-Free Tunable Angular Propagation Characteristics Based on Edge States and Its Potential in Sensing

Bao-Fei Wan, Hai-Ning Ye, and Hai-Feng Zhang

***Abstract*— In this article, by combining the epsilon-near-zero (ENZ) edge state of the InSb material and the photonic bandgap (PBG) edge state of photonic crystals (PCs), the angular transparent window (ATW) in a specific angle range is excited. The ATW is pattern-free, meaning that the same windows can be excited without being affected by polarization. The left edge of ATW is controlled by the refractive index of the PC dielectrics, while the right one can be adjusted by the temperature, and the two edges can be independently regulated. ENZ edge state maintains linear variation in both frequency and angle domains, which provides the possibility for the sensing design in two freedoms. Frequency-domain detection can be used for a large measurement range while angle-domain detection is equipped with extremely high sensitivity. In addition, the proposed structure has the capability of multivariable sensing to measure different physical quantities. For temperature detection, the maximum measurement range and the maximum sensitivity are 260–350 K and 26.678°/K, respectively, while for refractive index sensing, the corresponding values are 1.3–1.9 and 97.9°/RIU, respectively. In addition, due to the high sensitivity of the angular refractive index sensor, the proposed structure can also be utilized to detect citrate solution. The sensors of two freedoms based on the ENZ edge state provide the possibility to realize the detection of a large range, high sensitivity, and multiple functions at the same time.**

***Index Terms*— Angular transparent window (ATW), detection of two freedoms, edge states, edge-independent control, multivariable sensors.**

## I. Introduction

IN THE research of electromagnetics and optics, the problem of energy transmission of angle systems has always been an important basic technology [1], [2], and it is also a scientific challenge. Frequency, polarization, and propagation direction are the basic properties of a plane wave. The investigations on frequency systems and polarization regimes have been quite common, and the technologies have become increasingly mature, but the research on angle systems is relatively slow. The angle selection system means that the system allows the energy of a specific angle to pass through, while the energy of other angles is completely reflected. Based on these properties, the angle selection system has great application potential in the fields of angle filtering [3], radar anti-jamming [4], solar energy acquisition [5], privacy protection [6], edge enhancement [7], and optical imaging [8]. Some technical means have been used to explore the basic peculiarities of angle selection systems, such as the Fabry–Perot cavity [9], [10], [11], Brewster angle principle [12], [13], [14], anisotropic materials [15], [16], and photonic bandgap (PBG) [17], [18]. Fabry–Perot cavity technology is suitable for generating small-angle windows, and the selectivity is not very high. Brewster angle principle and anisotropic materials can generate a window with a certain angle and provide a large working bandwidth, but they are often polarization-sensitive and have weak selectivity. PBG structures possess excellent angle selectivity and overcome the defect of polarization sensitivity, but the adjustability of the angle window needs to be improved.

Some excellent research on angle propagation has been explored by predecessors. They are usually aimed at expanding bandwidth, overcoming polarization dependence, enhancing selectivity, or simplifying the structure. Shen et al. [19] realized the wideband angle selection structure through the photonic crystals (PCs) stack structure based on the Brewster angle principle, generating the angle window of TM wave, but the angle selectivity is weak. To achieve polarization insensitivity and improve angle selectivity, Lizuka et al. [20] proposed to use the edge topology of PBG to achieve angle filtering. Due to the frequency selection characteristics of the structure itself, the angle window inherently starts from 0°, and the tunability needs to be enhanced. Based on the Brewster angle principle, Qu et al. [21] introduced a half-wave plate structure into the structure so that the TE wave can also generate angle windows, but the selectivity is also slightly insufficient. Huang et al. [22] realized the angle selection peculiarity by using the uniaxial dielectric magnetic plate, greatly simplifying the complexity of the structure, while there is still room for improvement in the working bandwidth and tunability. Tian et al. [23] achieved a small-angle polarization-insensitive angle window by using defective PCs and verified its application in far-field projection through experiments. It can be observed that previous studies have mainly focused on bandwidth, polarization, selectivity,

Manuscript received 2 May 2023; revised 24 July 2023; accepted 1 September 2023. Date of publication 11 September 2023; date of current version 30 October 2023. This work was supported by the Postgraduate Research and Practice Innovation Program of Jiangsu Province under Grant KYCX23_1004. *(Corresponding author: Hai-Feng Zhang.)*

The authors are with the College of Electronic and Optical Engineering and the College of Flexible Electronics (Future Technology), Nanjing University of Posts and Telecommunications, Nanjing 210023, China (e-mail: hanlor@163.com).

Color versions of one or more figures in this article are available at https://doi.org/10.1109/TAP.2023.3312583.

Digital Object Identifier 10.1109/TAP.2023.3312583

and structure. Nevertheless, in angle selection systems, the flexibility and pattern-free features of angle windows are also very important. For the structure proposed by predecessors, the polarization separation is inevitable even if the polarization dependence is overcome, but the pattern-free characteristic is indispensable in the field of privacy protection and antenna radiation.

As one of the commonly used sensors, optical sensors have always been a momentous research topic [24], [25], [26], [27]. PC sensors play an important role in many fields, such as environmental monitoring, chip processing, process manufacturing, and product testing, which are favored by scholars because of their high sensitivity, large measurement range, small size, and easy integration [28], [29], [30], [31]. The existing PC sensor principles include optical Tamm state, surface plasmon polariton, defect mode, Fano resonance, and so on. InSb materials have also become a choice for PC devices in recent years due to their unique optically adjustable properties. Unlike metals, the plasma frequency of InSb material is affected by ambient temperature because its intrinsic carrier concentration is controlled by temperature [32], [33]. Therefore, using the optical features of InSb, it is often introduced into the photonic structure as a unit for sensing design. Traditional optical sensor technology is often devoted to the detection of a single target. However, faced with the complex and changeable external environment and the requirements for the miniaturization of devices, multivariable detection has gradually become a research hotspot. During the study, researchers found that the number of targets detected and the basic performance of the sensor are often in conflict. Sometimes sensitivity or measurement range is sacrificed to expand the measurement object. Therefore, realizing multivariable sensing is always a problem that researchers need to overcome to satisfy the large measurement range and high sensitivity.

In this article, the epsilon-near-zero (ENZ) edge state of InSb and the PBG edge state are designed to control the two edges of the angular transparent window (ATW) to overcome the untunable shortcoming of the traditional ATWs. The two edges are independently regulated by the temperature and refractive index of the medium. Similar ATWs can be simulated by the TM and TE waves simultaneously without polarization dependence and polarization separation phenomena, which are defined as pattern-free. The edge state of the ENZ structure is linearly dependent on the external environment and exists in both frequency and angle domains. Therefore, a detection method based on two freedoms is proposed to achieve the phenomenon of large measurement range and high sensitivity respectively, which is suitable for different occasions. When the analyte depends on the measurement range, then frequency-domain detection can be used, and if sensitivity depends, then angle-domain detection is appropriate. In addition, the detection of two freedoms can also be used to measure the temperature and refractive index of the background medium at the same time, which caters to the demand of multivariable sensing. To verify the resolution of the angular refractive index sensor, citrate solutions are selected for analysis.

## II. Design of the Proposed ATW

The proposed ATW is described in Fig. 1. The right edge of the ATW is controlled by the ENZ structure, and the left edge is operated by the PC component. The combination of ENZ and PC structures induces the ATW. The ENZ structure consists of dielectrics InSb and air, and its sequence is $(InSb_2\text{-}Air)^3\text{-}InSb_1\text{-}(Air\text{-}InSb_2)^2$, where $InSb_1$is the host structure and the others are antireflection structures (AFS). Dielectrics $InSb_1$ and $InSb_2$ are the same material, but their thicknesses are different. The PC structure is composed of dielectrics A–C, and its arrangement belongs to $(A_2C)^2(A_1B)^{45}(CA_2)^2$, in which $(A_1B)^{45}$is the host structure and the elements on both sides are AFS. Similarly, $A_1$ and $A_2$ have different thicknesses, but the same medium. The host structure is used to generate the angle selection phenomenon, while the AFS is responsible for suppressing the reflection resonance in the ATW.

Among them, the refractive indexes of dielectrics A–C and air are $n_A = 3.3$, $n_B = 1.45$, $n_C = 2.15$, and $n_{air} = 1$, respectively, and the thicknesses are in turn $d_{A1} = 52\ \mu$m, $d_B = 37.7\ \mu$m, $d_C = 2.26\ \mu$m, $d_{A2} = 33.9\ \mu$m, and $d_{air} = 8\ \mu$m. For the convenience of expression, only the refractive index of the medium is given here, which is a common expression in PC systems [19], [21]. Of course, these media can be found in nature or synthesized artificially, but the design of materials is not the focus of this article [19], [21]. Therefore, the specific details of materials are not studied in depth in this article.

In the terahertz (THz) region, the dielectric function model of InSb can be simplified to a Drude model [34]

$$\varepsilon = \varepsilon_\infty - \frac{\omega_p^2}{\omega^2 + i\omega\gamma} \tag{1}$$

where $\varepsilon_\infty = 15.68$ is the high-frequency permittivity and $\omega_p = (e^2N/\varepsilon_0/m^*)^{1/2}$ is the plasma frequency. $\varepsilon_0$ means the vacuum dielectric constant and $e$ is the electronic power. $m$ stands for the electronic quality and $m^* = 0.015$ m. $\omega = 2\pi f$ indicates the angular frequency of the incident wave and $f$ is the frequency. $\gamma$ is the damping constant. Since $\gamma$ is much less than $\omega$ in the THz region, $\gamma$ can be approximately equal to 0 [34], [35], [36], [37]. $N$ is the intrinsic carrier density, which is written as

$$N = 5.76 \times 10^{20} Ta^{1.5} \exp[-0.26/(2 \times 8.625 \times 10^{-5} \times Ta]. \tag{2}$$

$Ta$ is the temperature. The thicknesses of $InSb_1$ and $InSb_2$ layers are $d_{InSb1} = 350\ \mu$m and $d_{InSb2} = 13\ \mu$m, respectively. The energy propagation between layers is described by the transfer matrix method [36]. The transmittance and reflectance are denoted by $T$ and $R$, respectively.

The calculation formula of the dispersion curve $kd$ is shown in (3), where $\delta$ is the phase and $\eta$ is the admittance. The subscripts $a$ and $b$ mean the name of the medium, $\varepsilon$ is the dielectric constant, $h$ indicates the thickness, and $\theta$ is the propagation angle.

This formula is suitable for periodic PC structures with a large number of periods. For our proposed PC structure,

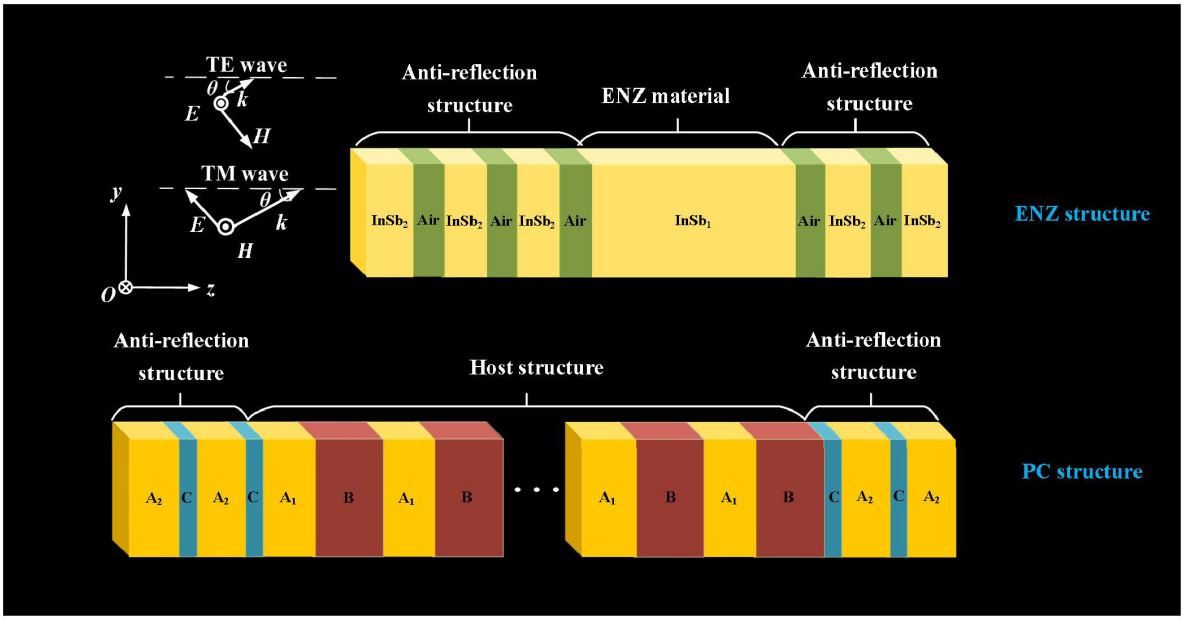


Fig. 1. Proposed ATW diagram. The incident wave propagates in the direction of $+z$ and the angle $\theta$ between the wave vector $k$ and the $+z$-axis. In the propagation direction, the magnetic field component fails to exist in the TM wave, and the electric field component is not owned by the TE one.

the host structure affects the position of the angle, while AFS only affects the amplitude. $kd$ is calculated to observe the angular position, so only the host structure needs to be calculated

$$\cos kd = \cos\delta_a \cos\delta_b - \frac{1}{2}\left(\frac{\eta_a}{\eta_b} + \frac{\eta_b}{\eta_a}\right)\sin\delta_a \sin\delta_b. \quad (3)$$

For the TE wave

$$\delta_a = -\frac{\omega}{c}\sqrt{\varepsilon_a}h_a\cos\theta_a, \quad \delta_b = -\frac{\omega}{c}\sqrt{\varepsilon_b}h_b\cos\theta_b \quad (4)$$

$$\eta_a = \sqrt{\frac{\varepsilon_0}{\mu_0}}\sqrt{\varepsilon_a}\cos\theta_a, \quad \eta_b = \sqrt{\frac{\varepsilon_0}{\mu_0}}\sqrt{\varepsilon_b}\cos\theta_b. \quad (5)$$

For the TM wave

$$\delta_a = -\frac{\omega}{c}\sqrt{\varepsilon_a}h_a\cos\theta_a, \quad \delta_b = -\frac{\omega}{c}\sqrt{\varepsilon_b}h_b\cos\theta_b \quad (6)$$

$$\eta_a = \sqrt{\frac{\varepsilon_0}{\mu_0}}\sqrt{\varepsilon_a}/\cos\theta_a, \quad \eta_b = \sqrt{\frac{\varepsilon_0}{\mu_0}}\sqrt{\varepsilon_b}/\cos\theta_b. \quad (7)$$

The group velocity of light wave propagation in PCs is closely related to the PBG structure and dispersion properties. The group velocity in the band is finite. At the edge of the PBG, the group velocity decreases rapidly and tends to 0, and the light propagation has a significant band delay effect. When $kd$ tends to 0, the group velocity tends to 0, indicating that electromagnetic waves are difficult to propagate.

## III. Analysis and Discussion

First, in Section III-A, the formation principle of pattern-free ATWs is explained and the distinctions of edge-independent regulation are studied. The left edge of ATW is affected by medium, while the right one is regulated by temperature. Second, in Sections III-B and III-C, the linear variation relationships of the ENZ edge state in the frequency domain and angle domain are found, and it is vulnerable to temperature and background medium. Hence, the multivariable sensing phenomena of the ENZ edge state are studied. For both temperature sensing and refractive index sensing, frequency-domain detection has a large measurement range, while angle-domain measurement has a high sensitivity. In Section III-D, to verify the high resolution brought by the refractive index angle sensor, it can be observed that the citrate solutions of different components can be effectively identified. In Section III-E, the effects of common errors on the device are discussed.

### A. Pattern-Free Edge-Independent ATWs

For convenience, the edge state generated by the ENZ portion is called the ENZ edge state and the edge state generated by the PC structure is called the PBG edge state for short. For the TE wave, in Fig. 2(a), the dielectric constant of InSb changes from a negative state to a positive one. When $\varepsilon_{\mathrm{InSb}}$ is 0, the energy of electromagnetic wave changes significantly from total reflection to strong transmission. During the transformation from 0° to 60°, the ENZ edge state produces a blueshifted phenomenon. The propagation characteristics of electromagnetic waves in an InSb medium are closely related to the phase change, and the phase is positively related to the cosine of the incident angle. When the incident angle is 0, the phase is the largest, and when the angle is increasing, the phase is decreasing. Then, the wavelength that can achieve optical path matching will also decrease, showing a blueshifted phenomenon. When the frequency is 2.65 THz, the energy jumps from transmission to reflection, which also means that there is a steep ENZ jump phenomenon in the angle domain. In Fig. 2(b), for the PBG edge state, during the transition of the incidence angle from 10° to 20°, the edge state of the PBG moves to the high-frequency area, and the state at 2.65 THz

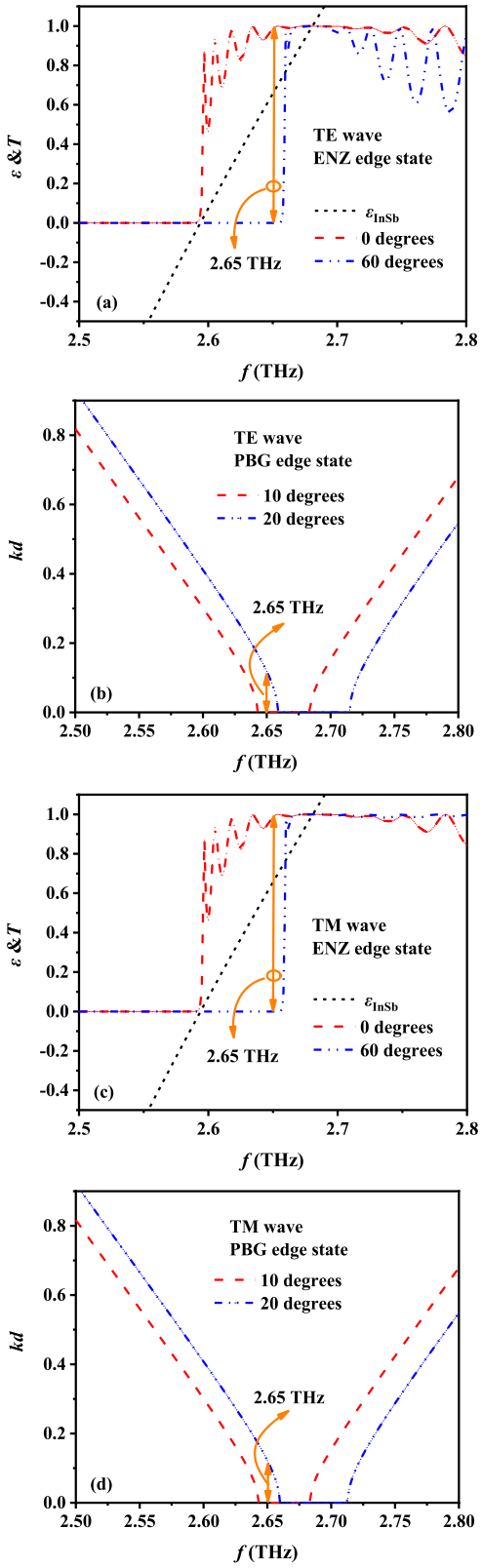


Fig. 2. Under the TE wave incidence, (a) variation trend of dielectric constant of InSb medium and the amplitude hopping of the ENZ edge state and (b) dispersion edges of the PBG edge state. Under the TM wave incidence, (c) variation trend of dielectric constant of InSb medium and the amplitude hopping features of the ENZ edge state, and (d) dispersion edges of the PBG edge state.

jumps from total reflection to transmission. In the case of the TM wave incidence, in Fig. 2(c), the ENZ edge state will also blueshift during the transition of the incident angle from 0° to 60°, and the electromagnetic wave energy is faced with the transition from high transmission to strong reflection at 2.65 THz. In Fig. 2(d), the hurricane of amplitude state of PBG edge state will also occur in the region of 10°–20°.

To more clearly demonstrate the propagation of electromagnetic wave energy near the edge states, the electric field energy distribution circumstances of $f = 2.65$ THz are provided. In Fig. 3(a), for the ENZ edge state in the case of the TE wave, when $\theta$ is 0°, the entire structure presents extremely high electric field energy distribution, which means that electromagnetic waves can pass through the structure smoothly. However, at the incidence of 60°, the electric field is only displayed near the incident port, suggesting that the electromagnetic wave resonates with the structure only near the port and then is completely reflected and fails to pass through the structure. In Fig. 3(b), for the PBG edge state, if the incident angle is 10°, the electric field energy only exists near the port and is not fully reflected through the structure. When the incident angle is 20°, the whole structure is full of energy, which means that electromagnetic wave passes through the structure smoothly, resulting in a transmission phenomenon. Through the analysis of the TE wave, it is not difficult to find that the energy distribution of the two edge states is consistent with the frequency domain shown in Fig. 2(a) and (b). In Fig. 3(c) and (d), assuming that the TM wave is incident, the electric field energy distribution is similar to that of the TE one, so details will not be elaborated.

According to the above analysis for the host structure, the edge states will produce significant deviation at different angle incidences, so if the frequency-domain research is transferred to the angle domain, a steep edge selection phenomenon will also occur, as shown in Fig. 4(a)–(d). In addition, in Fig. 1, both the ENZ and PC structures have been added to AFS on both sides of the host structure. This is mainly to compensate for the transverse impedance of the host structure, to achieve the effect of impedance matching, fully suppress reflection, and increase transparency [20]. In Fig. 4(a) and (b), when the TE wave is incident without AFS, the structure itself will produce a strong resonance phenomenon, resulting in serious leakage of electromagnetic wave, and the introduction of AFS significantly makes up for the transmission gap of large angle. The final transmission energy of the ENZ edge state and PBG edge state reaches more than 85% in the entire ATW. In Fig. 4(c) and (d), if the TM wave is incident, even without AFS, the transmission of the electromagnetic wave is stronger than that of the TE wave. There is weak leakage at the ENZ edge state and the transmission energy of the PBG edge state is always higher than 85%. However, to maintain polarization independence, AFS is also introduced to enhance transparency. At the same time, no matter which polarization wave, the ENZ edge state, or the PBG edge state, the angle range of ATW and the selectivity of the edges will not be affected during the operation of AFS.

However, the addition of AFS is not arbitrary, and the appropriate refractive index and thickness need to be obtained through theoretical analysis [17], [38], [39]. The

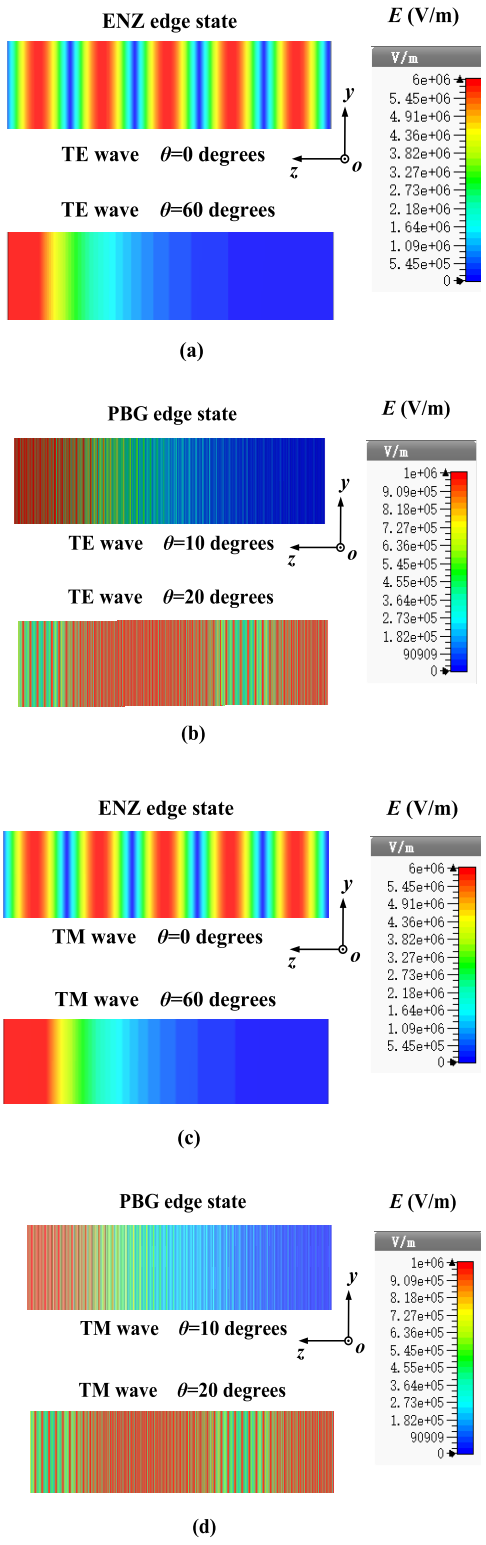


Fig. 3. $f = 2.65$ THz. Under the TE wave incidence, (a) energy states of the ENZ edge state at different angles and (b) energy states of the PBG edge state at different angles. Under the TM wave incidence, (c) energy states of the ENZ edge state at different angles and (d) energy states of the PBG edge state at different angles.

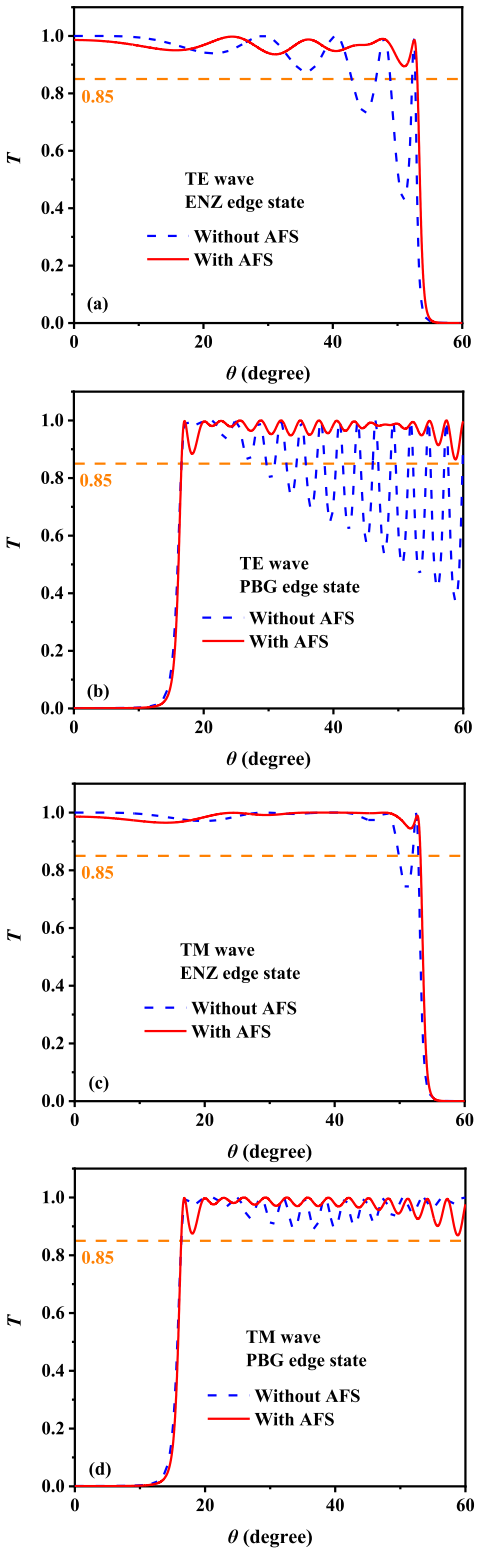


Fig. 4. $f = 2.65$ THz and $Ta = 300$ K, in the case of the incident TE wave, the effects of AFS on (a) ENZ edge state of ATW and (b) PBG edge state of ATW. In the case of the incident TM wave, the influences of AFS on (c) ENZ edge state of ATW and (d) PBG edge state of ATW.

air background, AFS, and host structure are considered as media 1–3, respectively. The wave vector $k_1 = (k_y, k_{x1}) = (n_1 k_0 \sin\theta, n_1 k_0 \cos\theta)$ comes from medium 1 with the refractive index of $n_1$. The thickness and refractive index of medium 2 are $d_2$ and $n_2$, in turn. In the case of $n_2$ determination, the thickness of the AFS becomes the key factor to suppress the reflection sufficiently. The total reflection of the whole system is composed of the reflection between layers superimposed

many times. It can be expressed as

$$r = r_{12} + t_{12}\phi_{23}\phi\left[\sum_{n=0}^{\infty}(r_{21}\phi_{23}\phi)^n\right]t_{21} = \frac{r_{12} + (t_{12}t_{21} - r_{12}r_{21})r_{23}\phi^2}{1 - r_{21}r_{23}\phi^2} \tag{8}$$

where, $r_{ij}$ and $t_{ij}$ refer to the reflection and transmission coefficient between $i$ and $j$ at the interface of the medium, respectively. $\Phi = e^{ikx2d2}$ and $k_{x2} = (n_2^2k_0^2 - k_z^2)^{1/2}$. Through Fresnel's theorem, $r_{ij}$ and $t_{ij}$ can be represented as

$$r_{ij} = \frac{X_j - X_i}{X_j + X_i}, \quad t_{ij} = \frac{2X_j}{X_j + X_i}. \tag{9}$$

$X_i$ describes the transverse impedance of dielectric $i$. For the TE wave, $X_i$ means the transverse impedance of dielectric $i$ and $X_i = Z_i = k_0\mu_i/k_{x,i}$. As to the TM one, it is defined as $X_i = Z_i = k_0\varepsilon_i/k_{x,i}$. $r_{12} = -r_{21}$ and $t_{12}t_{21} - r_{12}r_{21} = 1$ are constant in (9); hence, it can be simplified as

$$r = \frac{r_{12} + r_{23}\phi^2}{1 + r_{12}r_{23}\phi^2}. \tag{10}$$

The parameters $n_2$ and $d_2$ of the AFS can be obtained by the calculation of the above formula. If the lossless of the AFS is quite weak, $|\phi| = 1$ is satisfied, and the two core factors are: one is the moduli of $r_{12}$ and $r_{23}$ that are equal and the other is that $d_2$ meets the condition as follows:

$$d_2 = \frac{\arg r_{12} - \arg r_{23} + (2m+1)\pi}{2k_{x2}} \tag{11}$$

in which $m$ is an integer and arg $x$ represents the argument of the complex number $x$. For the sake of avoiding the internal resonances in the AFS from breaking its antireflective properties for some angles of incidence, we should choose the smallest $m$ when we make sure that $d_2$ is a positive value. In our proposed design, the structural settings of AFS also satisfy this mechanism.

In Fig. 5(a), under the case of the TE wave, when the PBG structure acts alone, the energy is completely reflected in the range of incidence angle less than 10°. In the range of 10°–20°, the energy has a transition from strong reflection to high transmission. The selectivity near the critical angle is significant, and the transmissivity is higher than 85%. If only the ENZ structure is working, the energy starts to reveal a transmission state from 0° to a total reflection phenomenon in the area of 50°–60°. While maintaining a good angle selectivity, the transmissivity near the critical angle is also higher than 85%. Naturally, it is assumed that the combination of PBG and ENZ structures will create an ATW with double edges. The composite structure forms an angle window with transmissivity higher than 85% in the range of 16.8°–53.1°. Similarly, in Fig. 5(b), when the TM wave is incident, the PBG structure produces the change from reflection to transmission state in the area of 10°–20°, while the ENZ structure promotes the transition between transmission and reflection phenomenon in the range of 50°–60°, and the transmission amplitudes at the critical angle exceed 0.85. The ATW with 16.4°–53.3° appears after the combination of two structures. By comparison, it can

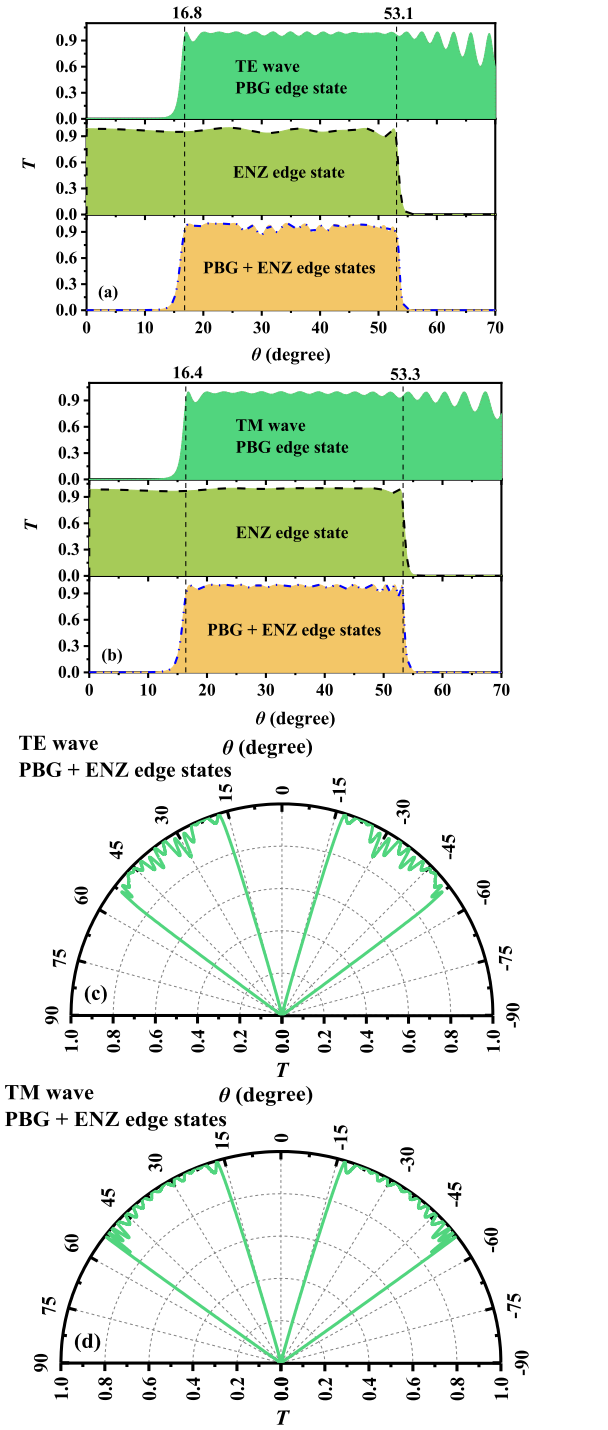


Fig. 5. Pattern-free ATWs under the sole action of PBG edge state or ENZ edge state and the ATWs after the combination of both under (a) TM wave and (b) TE wave. Direction selection diagrams of (c) TE wave incidence and (d) TM wave incidence.

be seen that the TE and TM waves can excite ATWs at the same time, and the ranges of ATWs are almost the same, which proves the pattern-free performance of the design. There are two main reasons for the formation of a pattern-free phenomenon. First, the appearances of PBG and ENZ edge states fail to depend on polarization. Second, the PBG edge state is responsible for generating the left edge, and polarization separation will not occur when the incident is at

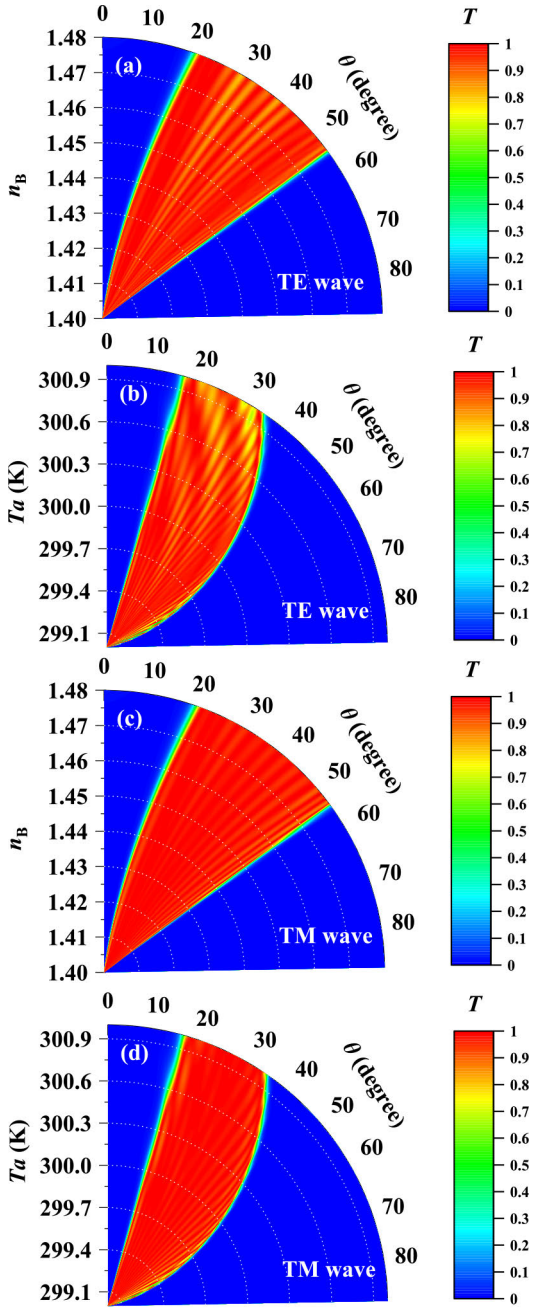


Fig. 6. In the case of the TE wave incidence, (a) regulation of $n_B$ on the left edge and (b) regulation of $Ta$ on the right edge. In the case of the TM wave incidence, (c) regulation of $n_B$ on the left edge and (d) regulation of $Ta$ on the right edge.

a small angle. The ENZ edge state promotes the right edge, and its dielectric constant distribution does not depend on polarization, so polarization separation will also not occur. To demonstrate the directional selection capability of the structure, the polar coordinate forms of Fig. 5(c) and (d) are illustrated. In angular systems, it is often necessary to get rid of the dependence on the polarization form of electromagnetic waves. Consequently, the proposed pattern-free structure provides a feasible design method for privacy protection from specific angles and directional selection of antennas. In addition, this property also means that the multivariable sensor designed in the following article can operate under any

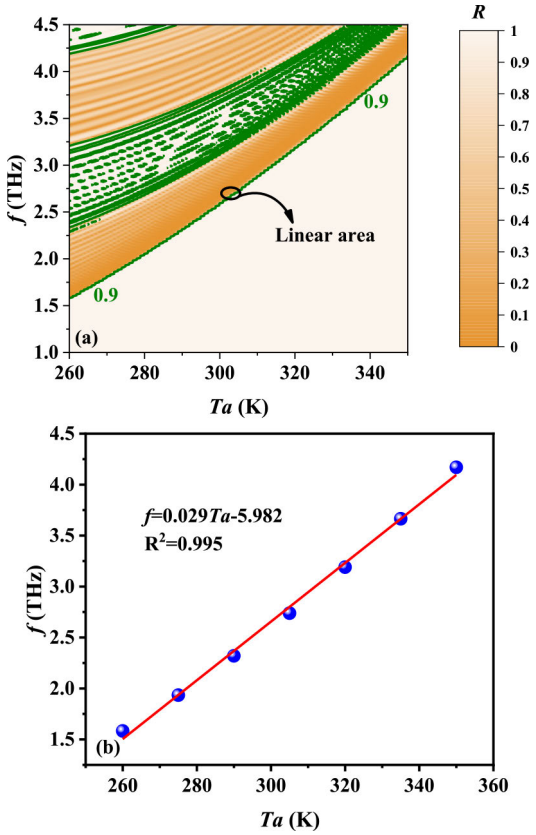


Fig. 7. $\theta = 0°$. (a) In the frequency domain, the variation of ENZ edge state with $Ta$ between 260 and 350 K. (b) Linear fitting relationship between frequency and temperature changes.

polarization of electromagnetic waves, improving the survival power of the device.

As analyzed in Fig. 4, the left and right edges of the ATW are controlled by the PC structure and ENZ component, respectively, meaning that the two sides can be adjusted independently, which is critical for the angle filters. In Fig. 6(a), if the refractive index of the position where dielectric B is located is adjusted and $n_B$ rises from 1.4 to 1.48, the left edge moves from 8.49° to 20.07°, while the right edge fails to produce any offset. When the TE wave is still the incident wave, in Fig. 6(b), if $Ta$ is modulated in the range of 299.4–301 K, only the right edge tends to increase from 33.41° to 66.54°. For the TM wave, similar manipulation results are also apparent. In Fig. 6(c), provided that $n_B$ changes, the range of the left edge is 8.3°–19.87°, while in Fig. 6(d), $Ta$ operates the right edge from 33.78° to 66.13°. Remarkably, no matter what the polarization wave is, the control of the edge of the ATW is independent of each other. This phenomenon benefits from the tunable properties of PBG and ENZ features. The adjustment of $n_B$ and $Ta$ obviously alters the position of PBG and ENZ edge states, thus affecting the critical jump position in the angle domain, resulting in the movement of the ATW.

### *B. Temperature Detection of Two Freedoms*

By exploring Fig. 6, it can be found that there is a linear transformation between the temperature and the ENZ

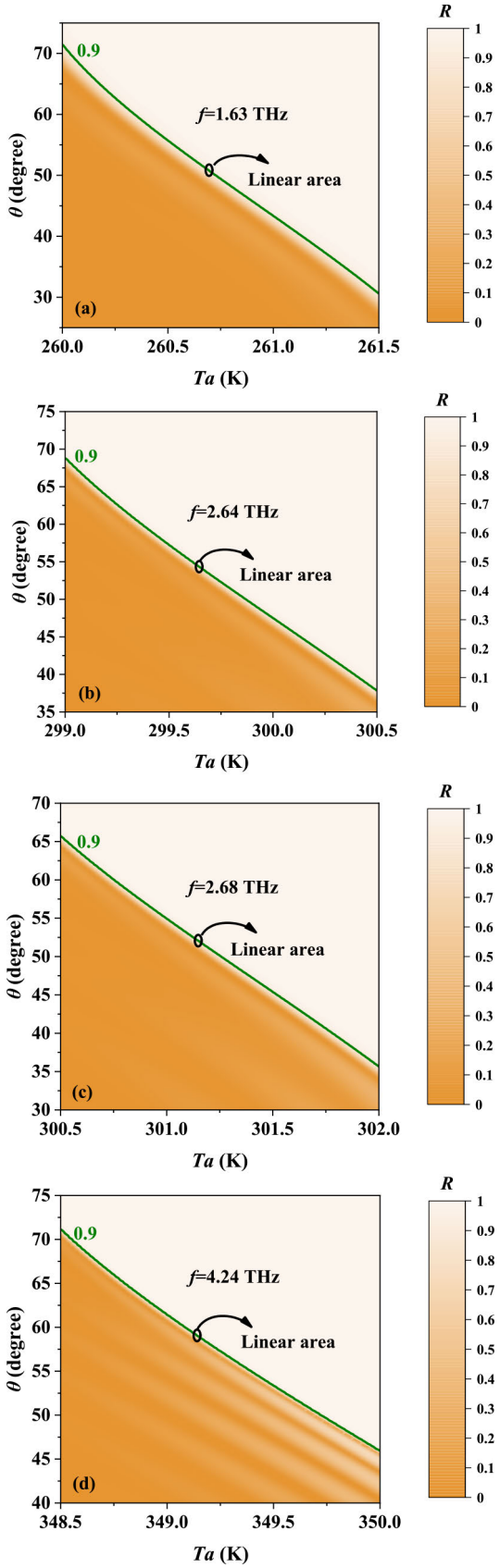


Fig. 8. Temperature detection range corresponding to specific frequency incidence. (a) $f = 1.63$ THz and $Ta$ belongs to 260–261.5 K. (b) $f = 2.64$ THz and $Ta$ belongs to 299–300.5 K. (c) $f = 2.68$ THz and $Ta$ belongs to 300.5–302 K. (d) $f = 4.24$ THz and $Ta$ belongs to 348.5–350 K.

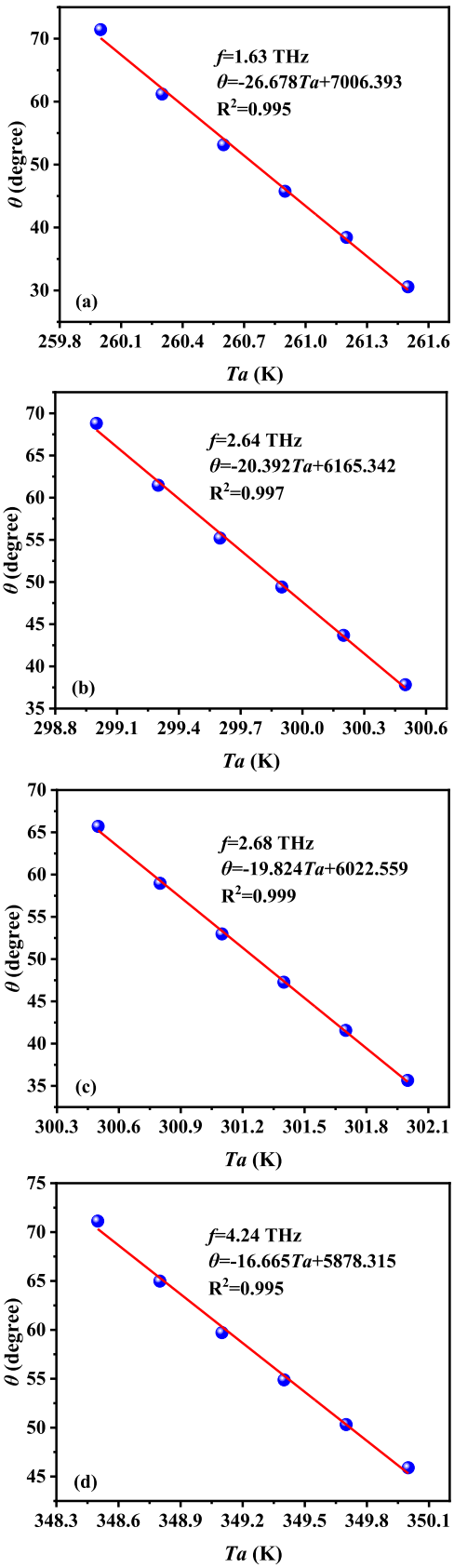


Fig. 9. In the angle domain, the linear fitting at specific frequencies: (a) $f = 1.63$ THz and $Ta$ belongs to 260–261.5 K, (b) $f = 2.64$ THz and $Ta$ belongs to 299–300.5 K, (c) $f = 2.68$ THz and $Ta$ belongs to 300.5–302 K, and (d) $f = 4.24$ THz and $Ta$ belongs to 348.5–350 K.

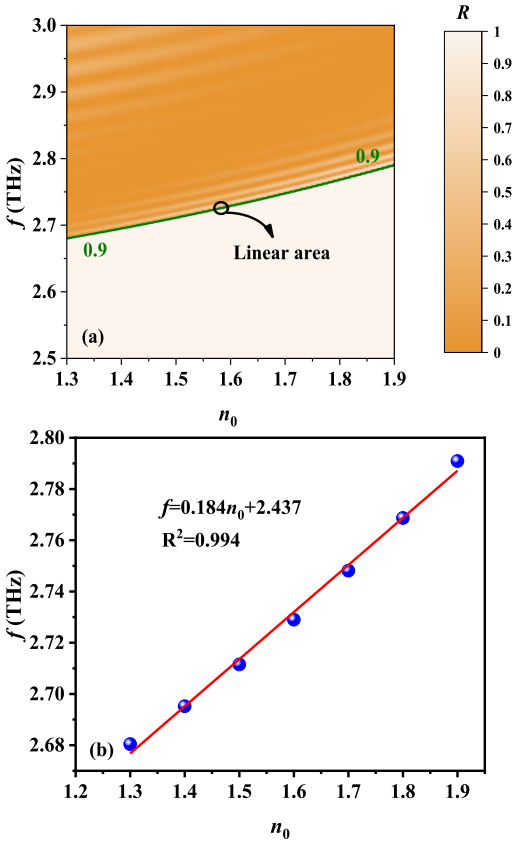


Fig. 10. $\theta = 50°$. (a) In the frequency domain, the variation of ENZ edge state with $n_0$ between 1.3 and 1.9. (b) Linear fitting relationship between frequency and refractive index changes.

edge state with extremely high sensitivity, which provides the possibility for temperature sensing. To reflect the sensing qualities, the reflectivity curve under the TE wave is used for observation. The ENZ edge state exists in two freedoms, and those are the frequency and angle domains, so the characteristics of temperature sensing are discussed. In Fig. 7(a), when the temperature increases from 260 to 350 K, the ENZ edge state adjusts linearly with the frequency and is always continuous. As shown by the green contour in the figure, the reflectivity of 0.9 is selected as the dependence of the sensor reading. In Fig. 7(b), if the temperature is 260, 275, 290, 305, 320, 335, and 350 K, the corresponding ENZ edge states fall on 1.583, 1.934, 2.32, 2.738, 3.19, 3.665, and 4.17 THz, respectively. After linear fitting of the temperature shift and resonance frequency, the fitting equation can be expressed as: $f = 0.029Ta - 5.982$, which also means that the sensitivity of the temperature sensor is 0.029 THz/K within the measurement range. At the same time, the variance $R^2$ of the fitting equation is 0.995. The closer the value is to 1, the higher the measurement accuracy of the sensor is. It can be seen that temperature detection in the frequency domain has a large measurement range. Therefore, for some environments, if a large measurement range is required, but a strong resolution is not required, frequency-domain detection can be selected.

At a certain frequency, the ENZ edge state of the angle domain also presents a linear trend. The extremely high sensitivity forces the temperature measurement range to be narrow, so the linear range of 260–350 K is divided into 60 segments, of which four segments are used for specific analysis. In Fig. 8(a), when the excitation frequency is 1.63 THz, the continuous linear range is 260–261.5 K, and the angle change is 71.44°–30.56°. In Fig. 8(b), when the resonance frequency is 2.64 THz, the linear change is maintained in the temperature range of 299–300.5 K, and the angle is reduced from 68.81° to 37.82°. In Fig. 8(c), when the excitation frequency is 2.68 THz, the continuous linear range is 300.5–302 K, and the angle change is 65.7°–35.65°. In Fig. 8(d), when the resonance frequency is 4.24 THz, the linear change is maintained in the temperature range of 348.5–350 K, and the angle is reduced from 71.12° to 45.89°.

In Fig. 9(a), if the temperature is 260, 260.3, 260.6, 260.9, 261.2, and 261.5 K, the corresponding ENZ edge states fall on 71.44°, 61.19°, 53.13°, 45.75°, 38.41°, and 30.56°, respectively. After linear fitting of temperature change and ENZ angle, the fitting equation can be expressed as: $\theta = -26.678Ta + 7006.393$, which also means that the sensitivity of the temperature sensor is 26.678°/K within the measurement range, that is to say, if the resolvable incident angle only needs to reach 0.1°, the temperature resolution will reach 0.0037 K, which is extremely sensitive to temperature detection. At the same time, the variance $R^2$ of the fitting equation is 0.995. In Fig. 9(b), when the temperature increases from 299 to 300.5 K with an interval of 0.3 K, the resonance angles are 68.81°, 61.46°, 55.2°, 49.4°, 43.67°, and 37.82°. The fitting equation is $\theta = -20.392Ta + 6165.342$, from which the sensitivity is equal to 20.392°/K. It is inferred from the sensitivity that if the incident angle alters by 0.1°, the temperature changes by 0.0049 K, which is also very subtle. In addition, a variance as high as 0.997 also implies high and deep measurement accuracy. In Fig. 9(c), provided that the temperature is severally 300.5, 300.8, 301.1, 301.4, 301.7, and 302 K, the corresponding ENZ edge states become 65.7°, 58.96°, 52.97°, 47.26°, 41.56°, and 35.65°, respectively. The linear fitting illustrates that the fitting equation can be written as $\theta = -26.678Ta + 6022.559$, representing that the sensitivity is 19.824°/K within the measurement range, that is to say, if the resolvable incident angle reaches 0.1°, the temperature resolution will reach 0.005 K. The variance $R^2$ of the fitting equation is equal to 0.999. In Fig. 9(d), when the temperature rises from 348.5 to 350 K with an interval of 0.3 K, the resonance angles are 71.12°, 64.98°, 59.71°, 54.88°, 50.31°, and 45.89°. The fitting equation is $\theta = -16.665Ta + 5878.315$, where the sensitivity belongs to 16.665°/K. It is inferred from the sensitivity that if the incident angle alters by 0.1°, the temperature changes by 0.006 K, which is also very subtle. In addition, a variance as high as 0.995 also implies high and deep measurement accuracy. It can be observed that after the frequency-domain detection is transferred to the angle-domain detection, the sensitivity has made a huge leap, and the worst resolution is 0.006 K, which leads to the reduction of the measurement range. In processes such as chip manufacturing, temperature control is usually fragile, so angle-domain detection can play a positive role.

TABLE I
SEGMENTED TEMPERATURE DETECTION DISTRIBUTION

| *Ta* (K) | *f* (THz) | $\theta=aTa+b$ | | $R^2$ | *Ta* (K) | *f* (THz) | $\theta=aTa+b$ | | $R^2$ |
|---|---|---|---|---|---|---|---|---|---|
| | | *a* | *b* | | | | *a* | *b* | |
| 260~261.5 | 1.63 | -26.678 | 7006.393 | 0.995 | 305~306.5 | 2.81 | -19.322 | 5956.964 | 0.999 |
| 261.5~263 | 1.66 | -25.671 | 6777.180 | 0.999 | 306.5~308 | 2.85 | -19.066 | 5904.296 | 0.999 |
| 263~264.5 | 1.7 | -26.291 | 6985.604 | 0.994 | 308~309.5 | 2.9 | -19.038 | 5927.700 | 0.999 |
| 264.5~266 | 1.73 | -25.025 | 6683.449 | 0.999 | 309.5~311 | 2.94 | -18.750 | 5863.595 | 0.999 |
| 266~267.5 | 1.77 | -25.404 | 6827.335 | 0.995 | 311~312.5 | 2.99 | -18.692 | 5876.581 | 0.999 |
| 267.5~269 | 1.8 | -24.650 | 6656.65 | 0.999 | 312.5~314 | 3.03 | -18.448 | 5824.601 | 0.999 |
| 269~270.5 | 1.84 | -24.572 | 6676.912 | 0.998 | 314~315.5 | 3.08 | -18.322 | 5815.092 | 0.999 |
| 270.5~272 | 1.88 | -25.246 | 6900.505 | 0.993 | 315.5~317 | 3.12 | -18.198 | 5799.54 | 0.999 |
| 272~273.5 | 1.91 | -23.766 | 6527.424 | 0.999 | 317~318.5 | 3.17 | -17.996 | 5764.714 | 0.999 |
| 273.5~275 | 1.95 | -23.642 | 6532.011 | 0.998 | 318.5~320 | 3.22 | -17.880 | 5756.500 | 0.999 |
| 275~276.5 | 1.99 | -23.796 | 6612.462 | 0.996 | 320~321.5 | 3.27 | -17.838 | 5771.451 | 0.999 |
| 276.5~278 | 2.03 | -24.108 | 6736.798 | 0.993 | 321.5~323 | 3.32 | -17.842 | 5800.897 | 0.998 |
| 278~279.5 | 2.06 | -22.738 | 6383.075 | 0.999 | 323~324.5 | 3.37 | -17.860 | 5834.690 | 0.998 |
| 279.5~281 | 2.1 | -22.494 | 6350.226 | 0.999 | 324.5~326 | 3.42 | -17.888 | 5871.602 | 0.997 |
| 281~282.5 | 2.14 | -22.296 | 6329.233 | 0.999 | 326~327.5 | 3.46 | -17.190 | 5665.625 | 0.999 |
| 282.5~284 | 2.18 | -22.116 | 6312.402 | 0.999 | 327.5~329 | 3.51 | -17.094 | 5660.588 | 0.999 |
| 284~285.5 | 2.22 | -21.918 | 6289.583 | 0.999 | 329~330.5 | 3.56 | -17.002 | 5656.417 | 0.999 |
| 285.5~287 | 2.26 | -21.702 | 6260.710 | 0.999 | 330.5~332 | 3.61 | -16.896 | 5647.160 | 0.999 |
| 287~288.5 | 2.3 | -21.468 | 6225.727 | 0.999 | 332~333.5 | 3.66 | -16.778 | 5633.442 | 0.999 |
| 288.5~290 | 2.34 | -21.224 | 6186.877 | 0.999 | 333.5~335 | 3.71 | -16.644 | 5613.867 | 0.999 |
| 290~291.5 | 2.38 | -21.002 | 6153.444 | 0.999 | 335~336.5 | 3.76 | -16.504 | 5591.733 | 0.999 |
| 291.5~293 | 2.42 | -20.794 | 6123.199 | 0.999 | 336.5~338 | 3.81 | -16.342 | 5561.627 | 0.999 |
| 293~294.5 | 2.46 | -20.632 | 6105.620 | 0.999 | 338~339.5 | 3.86 | -16.174 | 5528.870 | 0.999 |
| 294.5~296 | 2.5 | -20.586 | 6121.544 | 0.999 | 339.5~341 | 3.91 | -16.002 | 5494.123 | 0.999 |
| 296~297.5 | 2.55 | -20.386 | 6099.033 | 0.999 | 341~342.5 | 3.96 | -15.824 | 5456.702 | 0.999 |
| 297.5~299 | 2.59 | -20.078 | 6035.846 | 0.999 | 342.5~344 | 4.02 | -16.132 | 5590.159 | 0.998 |
| 299~300.5 | 2.64 | -20.392 | 6165.342 | 0.997 | 344~345.5 | 4.07 | -15.880 | 5526.585 | 0.998 |
| 300.5~302 | 2.68 | -19.824 | 6022.559 | 0.998 | 345.5~347 | 4.12 | -15.628 | 5462.160 | 0.998 |
| 302~303.5 | 2.72 | -19.574 | 5973.921 | 0.9997 | 347~348.5 | 4.17 | -15.384 | 5399.676 | 0.999 |
| 303.5~305 | 2.76 | -19.414 | 5951.972 | 0.999 | 348.5~350 | 4.24 | -16.665 | 5878.315 | 0.995 |

Due to the high detection sensitivity in the angle domain, the linear range is divided into 60 segments, with 1.5 K as a measurement range. Table I shows the overall measurement details ($f$: operating frequency, $a$: sensitivity, $b$: intercept, and $R^2$: variance). According to the current measurement technology, the angle variation of 0.1° is completely detectable. If such a standard is followed, the worst resolution in the whole measurement process will also reach 0.0065 K, which is of great significance for fine temperature sensing.

### C. Refractive Index Detection of Two Freedoms

In addition, the proposed detection technology of two freedoms is also perceptive to variation in the background medium and exhibits sensing potential in both the frequency domain and the angle domain. The refractive index $n_0$ of the background medium is taken as the analyte, and the changes in the air layer in the ENZ structure are consistent with those of the background medium. In Fig. 10(a), if $n_0$ extends from 1.3 to 1.9, then the peak line of 0.9 at the ENZ edge state will move toward the high frequency, from 2.680 to 2.791 THz, and the whole process is continuous. Obviously, the increase of $n_0$ shifts the equivalent ENZ resonance frequency of the structure, thus driving the phenomenon. In Fig. 10(b), if $n_0$ is successively 1.3, 1.4, 1.5, 1.6, 1.7, 1.8, and 1.9, the corresponding ENZ resonance points are 2.680, 2.695, 2.712, 2.729, 2.748, 2.769, and 2.791 THz. The fitting equation of frequency and refractive index can be expressed as: $f = 0.184n_0 + 2.437$, which also implies a sensitivity of 0.184 THz/RIU. Also, the

TABLE II
SEGMENTED REFRACTIVE INDEX DETECTION DISTRIBUTION

| $n_0$ (RIU) | $f$ (THz) | $\theta=an_0+b$ | | $R^2$ |
|---|---|---|---|---|
| | | $a$ | $b$ | |
| 1.3~1.4 | 2.73 | -97.900 | 198.626 | 0.992 |
| 1.4~1.5 | 2.75 | -86.760 | 191.148 | 0.994 |
| 1.5~1.6 | 2.78 | -88.160 | 203.692 | 0.993 |
| 1.6~1.7 | 2.81 | -85.400 | 208.510 | 0.994 |
| 1.7~1.8 | 2.85 | -90.840 | 228.898 | 0.992 |
| 1.8~1.9 | 2.89 | -91.271 | 239.833 | 0.992 |

linear fitting variance is 0.994. It is observed that the refractive index sensor has a wide measurement range in frequency-domain detection.

In the angle domain, due to the extremely high sensitivity of angle sensing, the measurement range is limited. Therefore, the linear range of 1.3–1.9 is divided into six segments, two of which are selected here for detailed analysis. In Fig. 11(a), $f = 2.73$ THz, the ENZ angle decays correspondingly from 71.74° to 61.89° on the premise that $n_0$ is in the range of 1.3–1.4. In Fig. 11(b), supposing that $n_0$ increases from 1.3 to 1.4 with an interval of 0.02, the resonance angles are 71.74°, 69.28°, 67.14°, 65.23°, 63.47°, and 61.89° in turn. The fitting of resonance angle position changing with refractive index is shown as $\theta = -97.9n_0 + 198.626$, revealing the sensitivity of 97.9°/RIU within the measurement range and $R^2$ of 0.992. In spectral detection, if the angle change of 0.1° is distinguishable, then the refractive index resolution can reach 0.0010. In Fig. 11(c), if $n_0$ belongs to 1.8–1.9, the operating frequency is 2.89 THz and the resonance angle falls between 66.72° and 75.91°. In Fig. 11(d), provided that $n_0$ is 1.8, 1.82, 1.84, 1.86, 1.88, and 1.9, the corresponding ENZ edge states become 75.91°, 73.6°, 71.61°, 69.84°, 68.21°, and 66.72°, respectively. The fitting equation is $\theta = -91.3n_0 + 239.833$, where the sensitivity takes the value of 16.665°/K and $R^2$ is equal to 0.992. Likewise, when the angle alters 0.1°, the refractive index resolution can reach 0.0011. Unlike frequency-domain detection, extremely high sensitivity forces the sensor to have a narrow measurement range, in return for strong resolution.

The wide measurement range applicable to the frequency domain is divided into six stages in the angle domain. The specific performance details are described in Table II ($f$: operating frequency, $a$: sensitivity, $b$: intercept, and $R^2$: variance). If the angle change of 0.1° is discernable, the resolution value will be lower than 0.0012. Thus, such fine refractive index sensing can be used for cell detection, virus analysis, and solution concentration measurement, and their refractive index changes are usually in the range of $10^{-2}$ or $10^{-3}$.

### *D. Angular Refractive Index Detection Used for Identifying Citrate Solutions*

With the development of science and technology, the research of the angle domain has been applied more and more [40], [41], [42], [43], [44], [45], [46], [47]. Due to the superior sensitivity of angular domain detection in refractive index sensing, it can be used for directional detection of the composition of citrate solutions. Citrate is composed of citric acid anions and metal cations and is widely used in the food and pharmaceutical industries [48], [49], [50]. If it is used as a food additive, it can be used as a formula for soft water drinks, a preservative for dairy products, and a sweetener for food to make the food taste better and promote appetite [48]. An appropriate amount of citrate is beneficial to the body and can enhance the normal metabolism of the body. If citrate is used as a drug, they have different functions, such as adjusting uric acid, treating kidney stones, inhibiting irritability, and alleviating gingival bleeding. However, excessive consumption will aggravate the burden of the stomach, lead to osteoporosis, and cause nervous system diseases [49]. Therefore, accurate control of the content of citrate is of great significance for the maintenance of human health. In the THz band [50], the average refractive indexes of Zn-Citrate, Ca-Citrate, Li-Citrate, and K-Citrate solutions are, respectively, $n = 1.65 \pm 0.03$, $n = 1.76 \pm 0.01$, $n = 1.89 \pm 0.01$, and $n = 1.88 \pm 0.03$.

In Fig. 12(a), since the average refractive index range of Zn-Citrate is 1.62–1.68, which falls within the range of 1.6–1.7, the operating frequency is selected as $f = 2.81$ THz according to Table II. When the distribution of $n$ is 1.62, 1.65, and 1.68, the critical angles are 70.08°, 67.39°, and 65.04°, respectively, which also means that the reasonable range of Zn-Citrate is 65.04°–70.08°. In Fig. 12(b), the average refractive index of Ca-Citrate is 1.75–1.77, which belongs to the detection range when the incident frequency is $f = 2.85$ THz. If $n$ increases from 1.75 to 1.77 and the interval is 0.01, the resonance angles are 69.66°, 68.8°, and 67.97° in order, and the accurate area is 67.97°–69.66°. In Fig. 12(c), the accurate range of Li-Citrate becomes 1.88–1.9, belonging to 1.8–1.9. At this time, the working frequency of $f = 2.89$ THz is appropriate. If the three values of $n$ are 1.88, 1.89, and 1.9 in turn, the critical angle decreases from 68.24° to 67.49° and then to 66.76°. Consequently, the response angle of Li-Citrate should cover the zone of 66.76°–68.24°. In Fig. 12(d), the normative area of K-Citrate is 1.85–1.91, and the same working frequency is selected as Li-Citrate. When $n$ is expanded from 1.85 to 1.91, the three values of its main distribution are 70.72°, 68.24°, and 66.06° in turn. Due to the

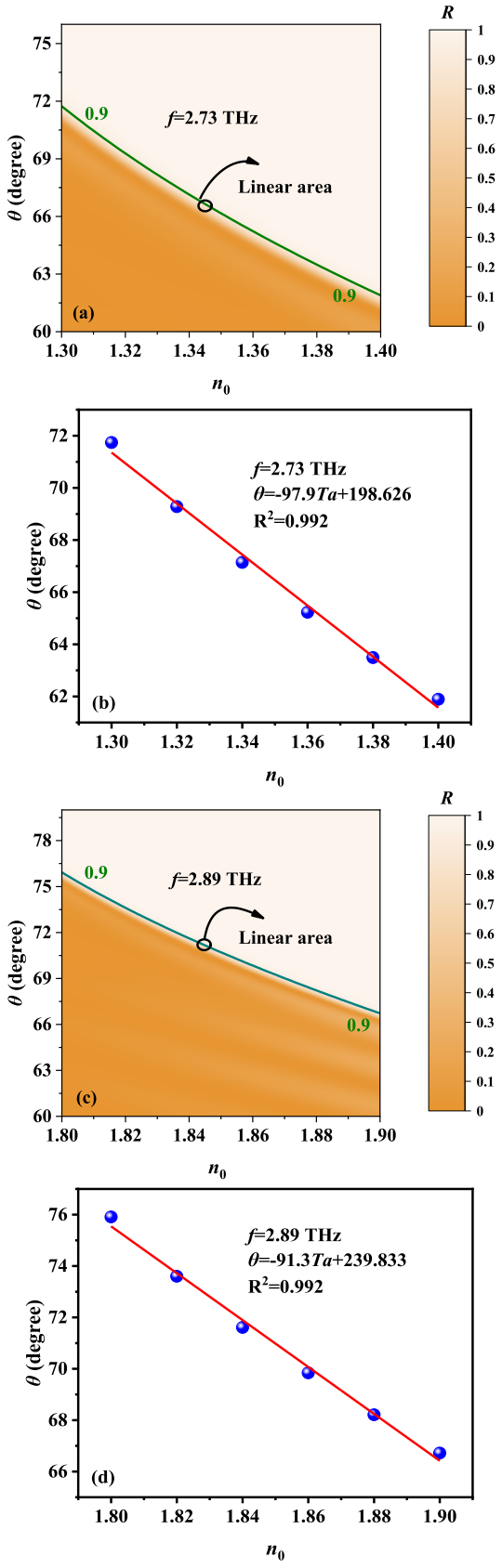


Fig. 11. In the case of $f = 2.73$ THz and $n_0$ belonging to 1.3–1.4, (a) three-dimensional planar graph and (b) linear fitting circumstances. In the case of $f = 2.89$ THz and $n_0$ belonging to 1.8–1.9, (c) three-dimensional planar graph and (d) linear fitting circumstances.

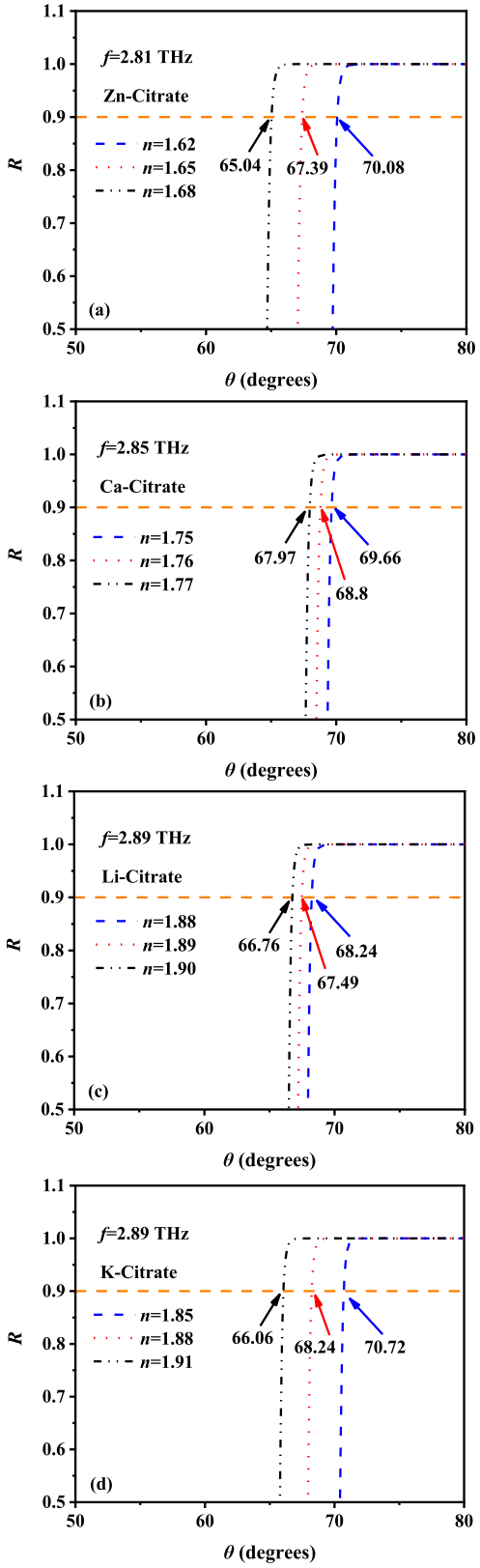


Fig. 12. In the angle domain, the difference of refractive indexes of citrate solutions can be used to identify different components. (a) Zn-Citrate, $f = 2.81$ THz and $n = 1.65 \pm 0.03$. (b) Ca-Citrate, $f = 2.85$ THz and $n = 1.76 \pm 0.01$. (c) Li-Citrate, $f = 2.89$ THz and $n = 1.89 \pm 0.01$. (d) K-Citrate, $f = 2.89$ THz and $n = 1.88 \pm 0.03$.

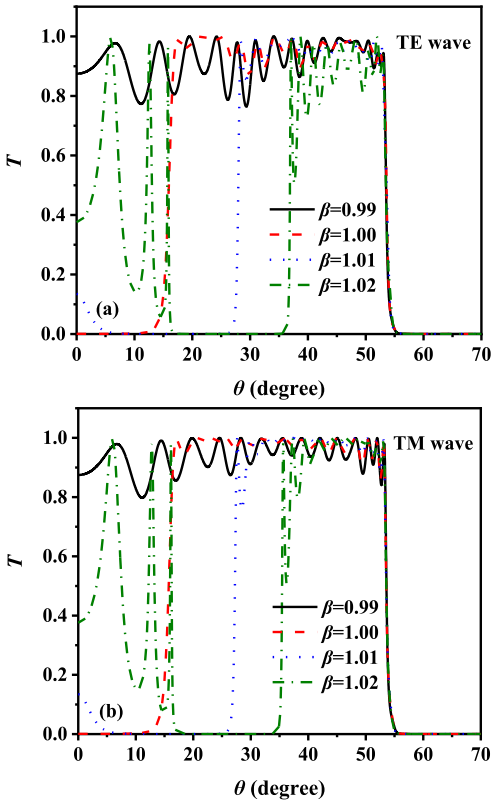


Fig. 13. Effects of error coefficient $\beta$ on ATW. (a) TE wave. (b) TM wave.

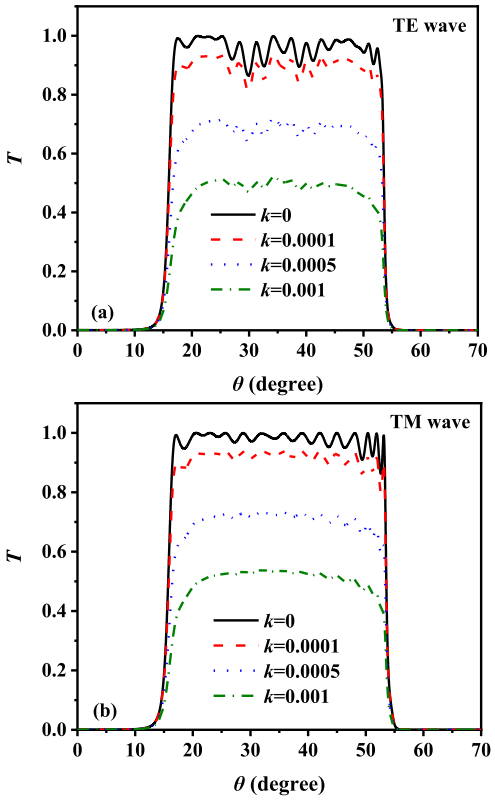


Fig. 14. Effects of extinction coefficient $k$ on ATW. (a) TE wave. (b) TM wave.

large refractive index distribution, the standard range is also wider from 66.06° to 70.72°. In general, profiting from the highly sensitive and segmented characteristics of angle-domain detection, citrate solutions with different components can be accurately distinguished and have corresponding standard intervals.

### *E. Effects of Process Errors*

In actual manufacturing, the most common errors are thickness error and loss error. For the convenience of expression, we define $\beta$ as the ratio of the thickness of the medium in the manufacturing process to the thickness of the medium in the ideal state. In Fig. 13, for any polarization wave, when $\beta$ is 0.99, the double-edge ATW becomes the single-edge ATW. As $\beta$ continues to increase, the PBG edge will move in a large angle direction, while the ENZ edge is not affected, resulting in a shrinking ATW. It can be seen that the thickness error only affects the PBG edge. Therefore, in the actual manufacturing process, the thickness of the PC structure needs to be precision machined to reduce the error as much as possible. In addition, for sensors based on ENZ edges, the performance of the sensor is not affected by thickness errors. It is worth noting that it is possible to reduce the impact of thickness error on PBG for the current lamellar structure processing technology [18].

To facilitate the expression, we will unify the extinction coefficients of all materials. In Fig. 14, it can be observed that for both TE and TM waves, the transmittance of ATW will decrease with the increase of extinction coefficient, and the greater the $k$ value, the more obvious the transmittance attenuation. Therefore, in practical applications, in order to meet the high transmittance, the extinction coefficient needs to be controlled below 0.0001. However, it is worth noting that the change of $k$ only affects the amplitude and will not pose a threat to the position of ATW. As a result, the introduction of loss does not affect the function of the sensor.

TABLE III
PERFORMANCE COMPARISON WITH PREVIOUS WORK

| Refs. | ATW | | | Sensor | |
|---|---|---|---|---|---|
| | Edge | Tunability | Pattern-free function | Single function | Dual function |
| 14 | Single | None | None | None | None |
| 18 | Single | None | None | None | None |
| 19 | Double | None | None | None | None |
| 20 | Single | None | None | None | None |
| 21 | Double | None | None | None | None |
| 51 | Single | None | None | Yes | None |
| This work | Double | Yes | Yes | None | Yes |

To more clearly demonstrate the innovations in this article, Table III is selected for performance comparison. In principle, different from the previous single-principle design, this article combines PBG technology and ENZ technology to get a double-edge angle window. Since the two edges are excited by different principles, they do not interfere with each other and have tunable characteristics. In addition, since ENZ edges are not affected by polarization and PBG edges are also almost unaffected by polarization at small angles, the proposed structure has pattern-free properties. Based on the vulnerability

of the ENZ edge to the external environment, a novel sensor based on the ENZ edge angle is designed. To solve the disadvantage of dual function sensor's incompatibility of sensitivity and measurement range, a two-degree-of-freedom detection technique is proposed to overcome this problem, which has not been reported in previous studies.

## IV. Conclusion

In this article, by ingeniously combining the ENZ and PBG edge states, a pattern-free ATW with two edges that can be independently adjusted is generated, which provides the possibility to design ATW from any angle. The ENZ edge state is controlled by temperature, while the PBG edge state is affected by the refractive index of the medium. At the same time, based on the linear relationship between the ENZ edge state and the external environment, the detection mechanism of two freedoms is proposed to achieve a wide measurement range and high sensitivity for multivariable sensors. For temperature detection, the maximum measurement range and maximum sensitivity are 260–350 K and 26.678°/K, respectively, while for refractive index sensing, the corresponding values are 1.3–1.9 and 97.9°/RIU, respectively. Citrate solutions detection is introduced to verify the resolution of the angular refractive index sensor. Therefore, we hope that the proposed structure can provide new ideas for improving ATW performance and multivariable sensors.

## References


[1] K. Yin et al., "Enabling manufacturable optical broadband angular-range selective films," *ACS Nano*, vol. 15, no. 12, pp. 19917–19923, Dec. 2021.

[2] J. Xu, J. Mandal, and A. P. Raman, "Broadband directional control of thermal emission," *Science*, vol. 372, pp. 393–397, Apr. 2021.

[3] Y. Shen, C. W. Hsu, Y. X. Yeng, J. D. Joannopoulos, and M. Soljačić, "Broadband angular selectivity of light at the nanoscale: Progress, applications, and outlook," *Appl. Phys. Rev.*, vol. 3, no. 1, Mar. 2016, Art. no. 011103.

[4] Y. Gao, B. Li, R. Wang, Q. Yan, J. Huangfu, and D. Ye, "Polarization-independent broadband angular selectivity based on anisotropic diamagnetic metamaterial," *IEEE Trans. Antennas Propag.*, vol. 70, no. 8, pp. 7306–7310, Aug. 2022.

[5] E. D. Kosten, B. M. Kayes, and H. A. Atwater, "Experimental demonstration of enhanced photon recycling in angle-restricted GaAs solar cells," *Energy Environ. Sci.*, vol. 7, no. 6, pp. 1907–1912, 2014.

[6] E. D. Kosten, J. H. Atwater, J. Parsons, A. Polman, and H. A. Atwater, "Highly efficient GaAs solar cells by limiting light emission angle," *Light, Sci. Appl.*, vol. 2, no. 1, p. e45, Jan. 2013.

[7] Y. Zhou, H. Zheng, I. I. Kravchenko, and J. Valentine, "Flat optics for image differentiation," *Nature Photon.*, vol. 14, no. 5, pp. 316–323, May 2020.

[8] A. Greenbaum et al., "Imaging without lenses: Achievements and remaining challenges of wide-field on-chip microscopy," *Nature Methods*, vol. 9, no. 9, pp. 889–895, Sep. 2012.

[9] Q. Qian, C. Xu, and C. Wang, "All-dielectric polarization-independent optical angular filter," *Sci. Rep.*, vol. 7, no. 1, p. 16574, Nov. 2017.

[10] K.-Y. Xu, X. Zheng, C.-L. Li, and W.-L. She, "Design of omnidirectional and multiple channeled filters using one-dimensional photonic crystals containing a defect layer with a negative refractive index," *Phys. Rev. E, Stat. Phys. Plasmas Fluids Relat. Interdiscip. Top.*, vol. 71, no. 6, Jun. 2005, Art. no. 066604.

[11] G. Liang, P. Han, and H. Wang, "Narrow frequency and sharp angular defect mode in one-dimensional photonic crystals from a photonic heterostructure," *Opt. Lett.*, vol. 29, no. 2, pp. 192–194, Jan. 2004.

[12] A. Alù, G. D'Aguanno, N. Mattiucci, and M. J. Bloemer, "Plasmonic Brewster angle: Broadband extraordinary transmission through optical gratings," *Phys. Rev. Lett.*, vol. 106, no. 12, Mar. 2011, Art. no. 123902.

[13] J. Guo, S. Chen, and S. Jiang, "Realization of optical broadband angular selectivity by the disordered structure," in *Proc. Asia Commun. Photon. Conf.*, 2017, Art. no. Su2A.137.

[14] H. Huang and Z. Shen, "Brewster lens with perfect wave refraction," *IEEE Trans. Antennas Propag.*, vol. 68, no. 8, pp. 6204–6213, Aug. 2020.

[15] R. E. Hamam, I. Celanovic, and M. Soljačić, "Angular photonic band gap," *Phys. Rev. A, Gen. Phys.*, vol. 83, no. 3, Mar. 2011, Art. no. 035806.

[16] Y. Shen et al., "Metamaterial broadband angular selectivity," *Phys. Rev. B, Condens. Matter*, vol. 90, no. 12, Sep. 2014, Art. no. 125422.

[17] B. Wan, H. Zhang, and P. Wang, "Nonreciprocal absorber with a narrow band of angular polarization sensitive regions based on a quasi-periodic structure," *Opt. Lett.*, vol. 46, no. 8, p. 1934, Apr. 2021.

[18] H. Tanaka, I. Takai, H. Fujikawa, and H. Iizuka, "Nearly polarization-independent angular filters consisting of one-dimensional photonic crystals realized in the visible region," *J. Lightwave Technol.*, vol. 36, pp. 2517–2523, Mar. 26, 2018.

[19] Y. Shen, D. Ye, I. Celanovic, S. G. Johnson, J. D. Joannopoulos, and M. Soljačić, "Optical broadband angular selectivity," *Science*, vol. 343, no. 6178, pp. 1499–1501, Mar. 2014.

[20] H. Iizuka, N. Engheta, and S. Sugiura, "Extremely small wavevector regime in a one-dimensional photonic crystal heterostructure for angular transmission filtering," *Opt. Lett.*, vol. 41, no. 16, pp. 3829–3832, Aug. 2016.

[21] Y. Qu et al., "Polarization-independent optical broadband angular selectivity," *ACS Photon.*, vol. 5, no. 10, pp. 4125–4131, Oct. 2018.

[22] H. Huang and Z. Shen, "Angle-selective surface based on uniaxial dielectric-magnetic slab," *IEEE Antennas Wireless Propag. Lett.*, vol. 19, no. 12, pp. 2457–2461, Dec. 2020.

[23] N. Tian, L. Feng, Y. Ren, R. Yu, X. Zhang, and T. Xu, "Polarization-insensitive optical angular filtration enabled by defective photonic crystals," *Appl. Phys. Lett.*, vol. 120, no. 24, Jun. 2022, Art. no. 241104.

[24] S. F. León-Luis, U. R. Rodríguez-Mendoza, E. Lalla, and V. Lavín, "Temperature sensor based on the $Er^{3+}$ green upconverted emission in a fluorotellurite glass," *Sens. Actuators B, Chem.*, vol. 158, no. 1, pp. 208–213, Nov. 2011.

[25] T. Q. Trung, S. Ramasundaram, B.-U. Hwang, and N.-E. Lee, "An all-elastomeric transparent and stretchable temperature sensor for body-attachable wearable electronics," *Adv. Mater.*, vol. 28, no. 3, pp. 502–509, Jan. 2016.

[26] K. Fabitha and M. S. R. Rao, "Biocompatible miniature temperature sensor based on whispering gallery modes of $Sm^{3+}$ activated ZnO optical micro-resonators," *Appl. Phys. Lett.*, vol. 118, no. 16, Apr. 2021, Art. no. 163104.

[27] Z. Zhu, D. Ba, L. Liu, L. Qiu, and Y. Dong, "Temperature-compensated distributed refractive index sensor based on an etched multi-core fiber in optical frequency domain reflectometry," *Opt. Lett.*, vol. 46, no. 17, p. 4308, Sep. 2021.

[28] M. F. O. Hameed, "Highly sensitive plasmonic photonic crystal temperature sensor filled with liquid crystal," *IEEE Photon. Technol. Lett.*, vol. 28, no. 1, pp. 59–62, Jan. 1, 2016.

[29] M. M. Abadla, H. A. Elsayed, and A. Mehaney, "Sensitivity enhancement of annular one dimensional photonic crystals temperature sensors with nematic liquid crystals," *Phys. Scripta*, vol. 95, no. 8, Jul. 2020, Art. no. 085508.

[30] A. Hocini and A. Harhouz, "Modeling and analysis of the temperature sensitivity in two-dimensional photonic crystal microcavity," *J. Nanophotonics*, vol. 10, no. 1, Feb. 2016, Art. no. 016007.

[31] Z. Baraket, J. Zaghdoudi, and M. Kanzari, "Investigation of the 1D symmetrical linear graded superconductor-dielectric photonic crystals and its potential applications as an optimized low temperature sensors," *Opt. Mater.*, vol. 64, pp. 147–151, Feb. 2017.

[32] S. Chen, F. Fan, X. Wang, P. Wu, H. Zhang, and S. Chang, "Terahertz isolator based on nonreciprocal magneto-metasurface," *Opt. Exp.*, vol. 23, no. 2, Jan. 2015, Art. no. 224884.

[33] B. Hu, Q. J. Wang, and Y. Zhang, "Slowing down terahertz waves with tunable group velocities in a broad frequency range by surface magneto plasmons," *Opt. Exp.*, vol. 20, no. 9, Apr. 2012, Art. no. 164178.

[34] Y. Ma et al., "Mach–Zehnder interferometer-based integrated terahertz temperature sensor," *IEEE J. Sel. Topics Quantum Electron.*, vol. 23, no. 4, pp. 1–7, Jul. 2017, doi: 10.1109/JSTQE.2017.2660882.

[35] A. Ghasempour Ardakani, T. Kalantari, and H. Nadgaran, "Tunable terahertz bistability with temperature in photonic crystals containing an InSb layer and coupled nonlinear defects," *Eur. Phys. J. B*, vol. 88, no. 9, p. 241, Sep. 2015.
[36] X. Dai, Y. Xiang, S. Wen, and H. He, "Thermally tunable and omni-directional terahertz photonic bandgap in the one-dimensional photonic crystals containing semiconductor InSb," *J. Appl. Phys.*, vol. 109, no. 5, Mar. 2011, Art. no. 053104.
[37] L. He et al., "One-way edge modes in a photonic crystal of semiconductor at terahertz frequencies," *Sci. Rep.*, vol. 8, no. 1, p. 8165, May 2018.
[38] W. Śmigaj and B. Gralak, "Semianalytical design of antireflection gratings for photonic crystals," *Phys. Rev. B, Condens. Matter*, vol. 85, no. 3, Jan. 2012, Art. no. 035114.
[39] C. Du et al., "An ultra-broadband terahertz metamaterial coherent absorber using multilayer electric ring resonator structures based on anti-reflection coating," *Nanoscale*, vol. 12, no. 17, pp. 9769–9775, May 2020.
[40] Y. Yuan et al., "A fully phase-modulated metasurface as an energy-controllable circular polarization router," *Adv. Sci.*, vol. 7, no. 18, Sep. 2020, Art. no. 2001437.
[41] A. H. Aly, S.-W. Ryu, H.-T. Hsu, and C.-J. Wu, "THz transmittance in one-dimensional superconducting nanomaterial-dielectric superlattice," *Mater. Chem. Phys.*, vol. 113, no. 1, pp. 382–384, Jan. 2009.
[42] C. Malek, A. H. Aly, S. Alamri, and W. Sabra, "Tunable PBGs with a cutoff frequency feature in Fibonacci quasi-periodic designs containing a superconductor material at THz region," *Phys. Scripta*, vol. 96, no. 10, Oct. 2021, Art. no. 105501.
[43] A. H. Aly and F. A. Sayed, "THz cutoff frequency and multifunction $Ti_2Ba_2Ca_2Cu_3O_{10}$/GaAs photonic bandgap materials," *Int. J. Modern Phys. B*, vol. 34, no. 10, Apr. 2020, Art. no. 30462.
[44] A. Natesan, K. P. Govindasamy, T. R. Gopal, V. Dhasarathan, and A. H. Aly, "Tricore photonic crystal fibre based refractive index sensor for glucose detection," *IET Optoelectronics*, vol. 13, no. 3, pp. 118–123, Jun. 2019.
[45] I. S. Amiri et al., "Tri-core photonic crystal fiber based refractive index dual sensor for salinity and temperature detection," *Microw. Opt. Technol. Lett.*, vol. 61, no. 3, pp. 847–852, Mar. 2019.
[46] A. H. Aly, A. Aghajamali, H. A. Elsayed, and M. Mobarak, "Analysis of cutoff frequency in a one-dimensional superconductor-metamaterial photonic crystal," *Phys. C, Supercond. Appl.*, vol. 528, pp. 5–8, Sep. 2016.
[47] A. H. Aly and D. Mohamed, "BSCCO/$SrTiO_3$ one dimensional superconducting photonic crystal for many applications," *J. Supercond. Novel Magnetism*, vol. 28, no. 6, pp. 1699–1703, Jun. 2015.
[48] D. Aguilar-Ramirez et al., "Association of kidney function with NMR-quantified lipids, lipoproteins, and metabolic measures in Mexican adults," *J. Clin. Endocrinology Metabolism*, vol. 106, no. 10, pp. 2828–2839, Sep. 2021.
[49] G. A. Block et al., "Effect of ferric citrate on serum phosphate and fibroblast growth factor 23 among patients with nondialysis-dependent chronic kidney disease: Path analyses," *Nephrology Dialysis Transplantation*, vol. 34, no. 7, pp. 1115–1124, Jul. 2019.
[50] X. Deng et al., "Terahertz metamaterial sensor for sensitive detection of citrate salt solutions," *Biosensors*, vol. 12, no. 6, p. 408, Jun. 2022.
[51] B.-F. Wan, H.-N. Ye, D. Zhang, and H. Zhang, "A variable refractive index sensor based on epsilon-near-zero spatial selection structure and its potential in biological detection," *New J. Phys.*, vol. 25, no. 2, Feb. 2023, Art. no. 023003.

**Bao-Fei Wan** was born in Jiangsu, China, in 1997. He is currently pursuing the bachelor's degree with the Nanjing University of Posts and Telecommunications, Nanjing, China.

His main research interests include directional regulation of electromagnetic waves, optical sensors, nonreciprocal devices, optical privacy protection, and optical anticounterfeiting.

**Hai-Ning Ye** was born in Hubei, China, in 2000. She is currently pursuing the bachelor's degree with the Nanjing University of Posts and Telecommunications, Nanjing, China.

Her main research interests include RCS reduction.

**Hai-Feng Zhang** was born in Jiangxi, China, in 1978. He received the M.Sc. degree in electronics science and technology from Nanchang University, Nanchang, China, in 2008, and the Ph.D. degree from the College of Electronic and Information Engineering, Nanjing University of Aeronautics and Astronautics, Nanjing, China, in 2014.

He is currently a Professor with the College of Electronic and Optical Engineering and the College of Flexible Electronics (Future Technology), Nanjing University of Posts and Telecommunications, Nanjing. His main research interests include computational electromagnetics, plasma photonic crystal, plasma stealthy, and electromagnetic properties of metamaterials.